Isentropic/shock compression and recovery methodology for materials using high-amplitude laser pulses

B.R. Maddox [a], H.-S. Park [a], C.-H. Lu [b], B.A. Remington [a], S. Prisbrey [a], B. Kad [b], R. Luo [c], M.A. Meyers [b],*

[a] Lawrence Livermore National Laboratory, 7000 East Avenue, Livermore, CA 94550, USA
[b] University of California, 9500 Gilman Drive, La Jolla, San Diego, CA 92093, USA
[c] General Atomics, 3483 Dunhill Street, San Diego, CA 92121-1200, USA

ABSTARCT

A new method of subjecting samples to high-amplitude laser pulses with durations in the ns range and recovering them for characterization is presented. It is applied to tantalum monocrystals and nanocrystals that are subjected to controlled and prescribed ramp loading configurations, creating a quasi-isentropic loading in the front that is retained up to 40 μm into the specimen. This is enabled by the use of a reservoir into which six laser beams impinge simultaneously, thereby creating plasma in a reservoir, from which the pulse is launched into the metal. This technique enables, with proper wave trapping devices, the recovery of the specimens for subsequent characterization. Successful experiments conducted in the Laboratory for Laser Energetics, U. of Rochester, generated pressure pulses with initial amplitudes ranging from 15 to 110 GPa and initial durations of ~3 ns. The quasi-isotropic loading minimizes thermal effects at the front surface. The compression history of the recovered samples is measured using velocity interferometry from an Al-coated LiF witness target on the same shot driven by a separate, but equivalent set of laser beams. These experimental measurements are compared with computations using a radiation hydrodynamics code. Recovered samples are investigated using optical, scanning, and transmission electron microscopy. The laser damage to the surface is characterized.

© 2013 Elsevier B.V. All rights reserved.

1. Introduction

Laser-compression is a powerful technique that can provide information about extreme material response to ultra-high pressures (up to and above 100 GPa) and strain rates ($> 10^8$), (e.g. [1]). In contrast with flyer-plate experiments which deliver a stress pulse that is initially square, the triangular pulse shape created by laser compression generates a pressure that decays continuously throughout the specimen. In flyer-plate experiments the initial pressure is maintained over a distance dictated by the initial duration of the top of the pulse.

The gas gun is a proven experimental tool that has enabled exploration of the extreme pressure regime for over fifty years. Recovery and diagnostic experiments have grown in sophistication. Reproducibility and control are excellent. The uniqueness of laser pulse compression in comparison with gas-gun and explosively-driven systems resides in the duration of the pulse, in the

nanosecond vs. microsecond domain. Thus, the regimes explored by the two techniques are different. There have been a number of recovery experiments conducted over the past twenty years at different pulsed laser facilities. However, compared to gas-gun experiments, recovery laser methodology is still not well established.

These recovered materials have been characterized using a host of post-shock techniques such as TEM, SEM, x-ray diffraction, and optical microscopy to determine the microstructural changes at various depths into the sample, essentially probing the material over a range of pressures, temperatures, and strain rates dictated by the pressure loading history and compression wave decay rate inside target [2–10]. Laser-driven isentropic compression experiments (ICE) furthermore allow the study of materials at even higher pressure and strain rate than traditional shock wave experiments where targets are subjected to extreme shock heating, often times to well above the melt temperature [8–13].

The Omega laser at the Laboratory for Laser Energetics (LLE) is well suited for such experiments and, with clever design, can provide multiple pieces of data per laser shot due to the large number of beams available (60) [14]. This paper describes an experimental set-up to soft-recover isentropically compressed Ta specimens while simultaneously measuring the laser drive using a VISAR witness target driven by a separate, but equivalent set of

* Corresponding author. Tel./fax: +1 858 534 4719.
E-mail addresses: maddox3@llnl.gov (B.R. Maddox), park1@llnl.gov (H.-S. Park), chiahuilu@gmail.com (C.-H. Lu), remington2@llnl.gov (B.A. Remington), prisbrey1@llnl.gov (S. Prisbrey), bkad@ucsd.edu (B. Kad), luorwga@gmail.com (R. Luo), mameyers@eng.ucsd.edu (M.A. Meyers).

laser beams [15]. Results from successful experiments based on this design are presented including characterization.

2. Experimental design

The design of the sample compression and soft-recovery scheme can be divided into three parts: the ICE (Isentropic Compression Experiment) drive package, recovery tube, and target chamber geometry. Each part will be described in detail in the following sections.

2.1. Isentropic compression experiment (ICE) drive

Schematics of the Ta sample and Al/LiF VISAR target assemblies are shown in Fig. 1. The targets were designed to use direct laser ablation to achieve quasi-isentropic compression (ICE drive). By using the LASNEX radiation hydrodynamics code [16], the peak pressure exerted on the target can be calculated. The design consists of a 20 µm thick polycarbonate ablator followed by a 180 µm thick CHBr (2%) "reservoir" separated from the Ta sample by a 300 µm vacuum gap. The gap and target components are supported by a Ta washer that has two 800 µm wide by 50 µm deep radial channels to allow evacuation of the gap between the reservoir and sample. A shock wave is launched into the ablator and is transmitted to the CHBr (2%) reservoir by the laser beam. The reservoir material unloads across the 300 µm vacuum gap as a plasma. This plasma then stagnates against the sample material, exerting a pressure that increases over a rise time interval (up to ~10 ns), thus compressing the sample.

Samples studied here are either Ta monocrystalline cylinders 3 mm in diameter and 3 mm thick, nanocrystalline Ta specimens in 3 mm disk (~0.6 mm thickness) form (Grain size~70 nm) (Fig. 1(a)), or LiF cylinders 3 mm in diameter and 0.5 mm thick coated with ~10 µm of Al (Fig. 1(b)) used as a drive witness sample.

Trapping of reflected waves is of importance in shock compression experiments to ensure that the deformation structure is generated by the primary compressive pulse and not by reflected pulses. In explosively-driven and gas-gun experiments the procedures are well established. DeCarli and Meyers [17] provide simple guidelines for the design of recovery systems in which the reflected waves are trapped. Gray [18–20] studied the effects of reflected waves in a systematic manner and concluded that the baseline design, consisting of rings for trapping the lateral release waves and a spall element at the rear of the specimen provided satisfactory momentum trapping, if properly dimensioned and machined. Computer simulations were used by Bourne and Gray [21] to design optimum recovery fixtures. In laser-driven experiments the pulse decays readily because of its short duration (~1–5 ns vs. ~0.1–2 µs in gas gun experiments). Nevertheless, the incorporation of wave trapping devices into the experimental setup is important. For this reason, a lateral momentum trap and a momentum cap were added to the nanocrystalline Ta specimens, which were disks with ~0.6 mm thickness. This is in essence an adaptation of the baseline design [19–21], albeit with much reduced dimensions. Five disks were stacked, inserted into a recovery tube, which acted as a lateral momentum trap, and backed by a momentum disk. The assembly is shown in Fig. 1(a).
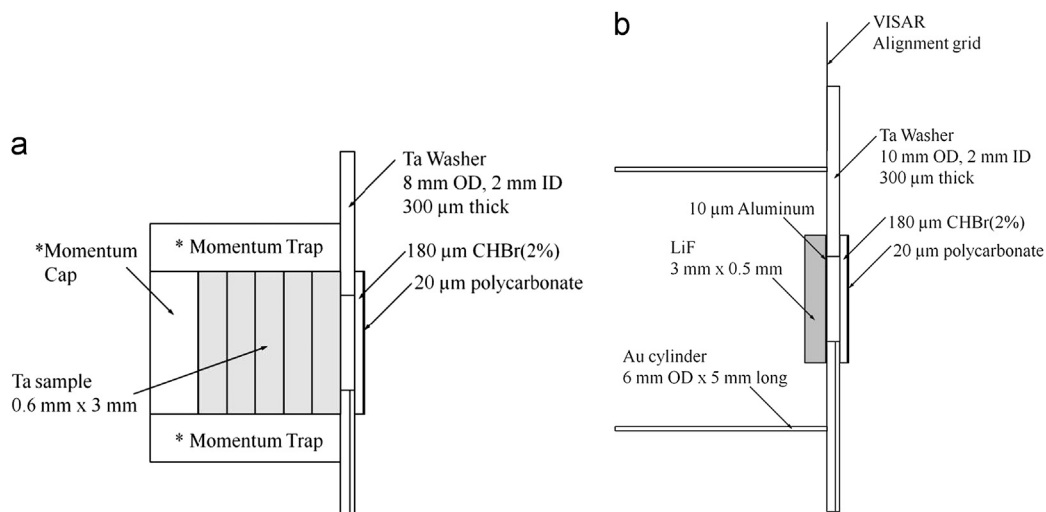

Fig. 1. ICE drive target designs for (a) Ta samples and for (b) the Al–LiF VISAR witness targets. *Optional 1 mm thick Ta momentum cap.
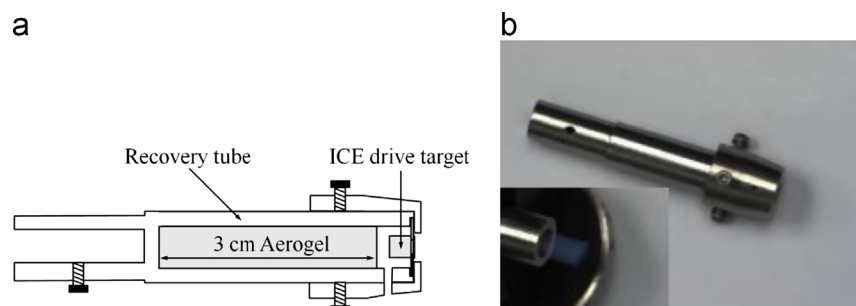

Fig. 2. (a) Cutaway drawing of the recovery tube target design showing the 3 cm long SiO$_2$ aero gel foam cylinder and the ICE drive target at the end and held in place by a stainless steel end cap; (b) Photograph of two recovery tubes, one fully assembled on the right; insert shows the recovery tube without cap or specimen assembly out of which aero gel cylinder protrudes.

2.2. Recovery tube

Sample recovery is accomplished by placing the sample target assembly at the end of a recovery tube filled with low-density SiO_2 aero gel. The recovery tubes consist of a stainless steel body with a 10 mm outer diameter, 6 mm inner diameter, and length of 54.8 mm. The target package is held securely at one end of the tube by a stainless-steel cap, which clamps down on the washer part of the
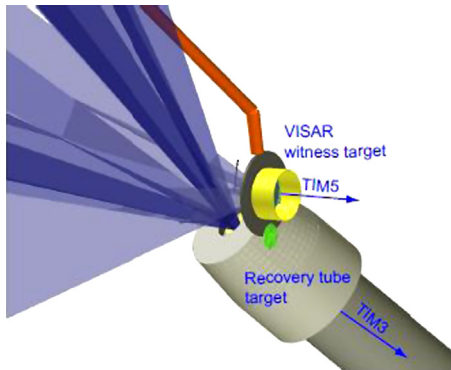

Fig. 3. Two-target geometry showing the Al–LiF VISAR witness target using the TIM5 VISAR and the recovery target mounted on the TIM3 target positioner.

target and is held in place by three set screws. This integrated sample/recovery tube is secured to the Omega target positioner using a Nova-style pin mount. Fig. 2(a) shows a cutaway of the recovery tube design. This design is similar in operation to that used in previous material recovery experiments by McNaney et al. at Omega [1]. Alignment of the entire assembly inside the target chamber is accomplished using two alignment fibers and the body of the recovery tube.

The interior of the recovery tube is fitted with a 3 cm long, 6 mm diameter 50 mg/cc SiO_2 aero gel foam cylinder. A photograph of a completed recovery tube is shown in Fig. 2(b) with an inset showing the aero gel cylinder partially inserted. The required foam density to achieve a soft recovery, with the sample arrested before reaching the end of the tube, was calculated using a "snowplow" compressibility model for an estimated target velocity of 284 m/s calculated from LASNEX [22,23].

2.3. Target chamber geometry

The Omega laser facility [24] in the Laboratory of Laser Energetics (LLE) is a 40 kJ UV 60 beam laser system with wavelength of 350 nm. The beam size can down to less than 1 mm diameter with pulse duration in nanosecond range. The experiment described in this paper was designed to drive multiple targets per laser shot, taking advantage of the large number of beams (60) available on the Omega laser. Only
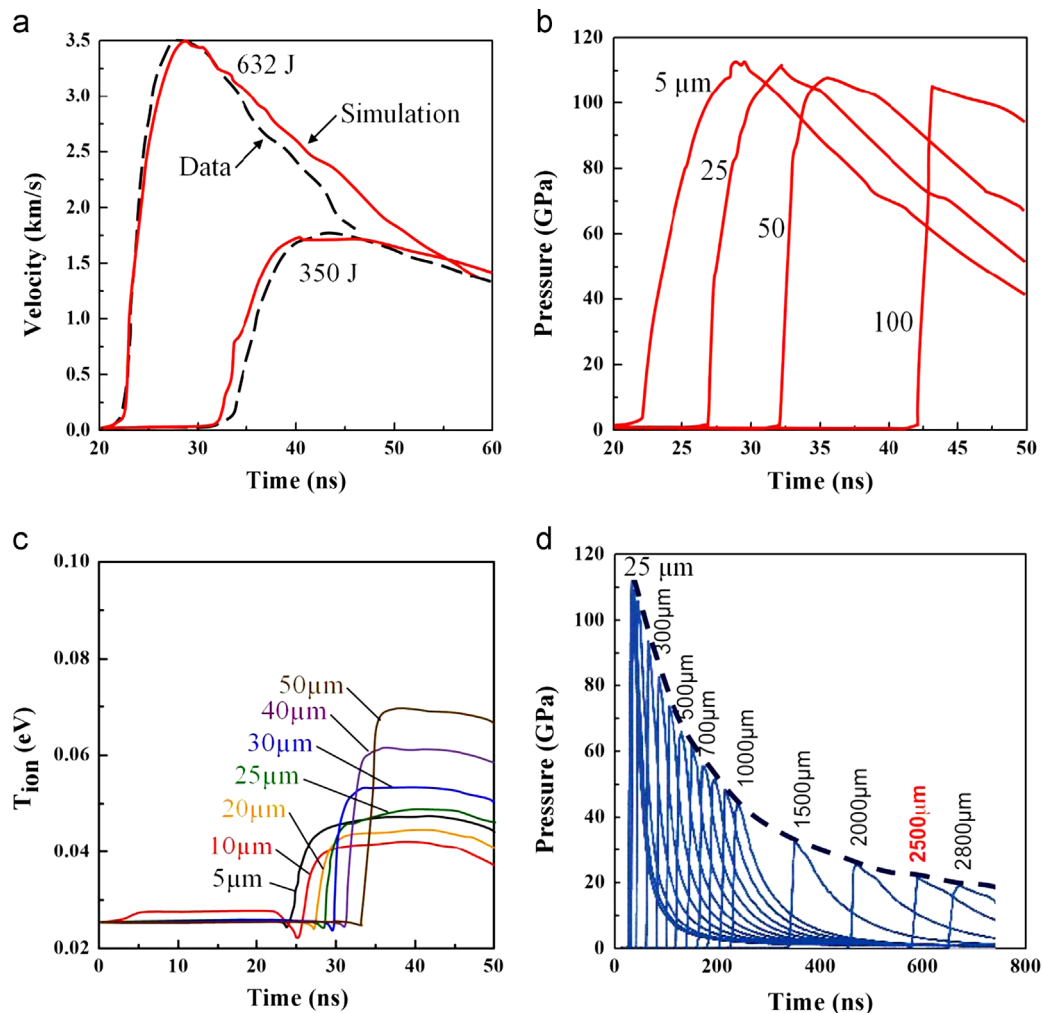

Fig. 4. (a) Comparison of the Al particle velocity measured by VISAR and simulated using 1D LASNEX for a high and low energy drive. Laser intensity scaling factors were 0.70 and 0.63 for the 632 and 350 J shots, respectively (b) Simulations of the pressure profiles inside the recovered Ta sample shot simultaneously with the 632J VISAR target at 5 μm, 25 μm, 50 μm, and 100 μm from the front (laser-side) and (c) ion temperature at a number of different depths. (d) Pressure vs. time at various depths into the target calculated using 1D LASNEX.
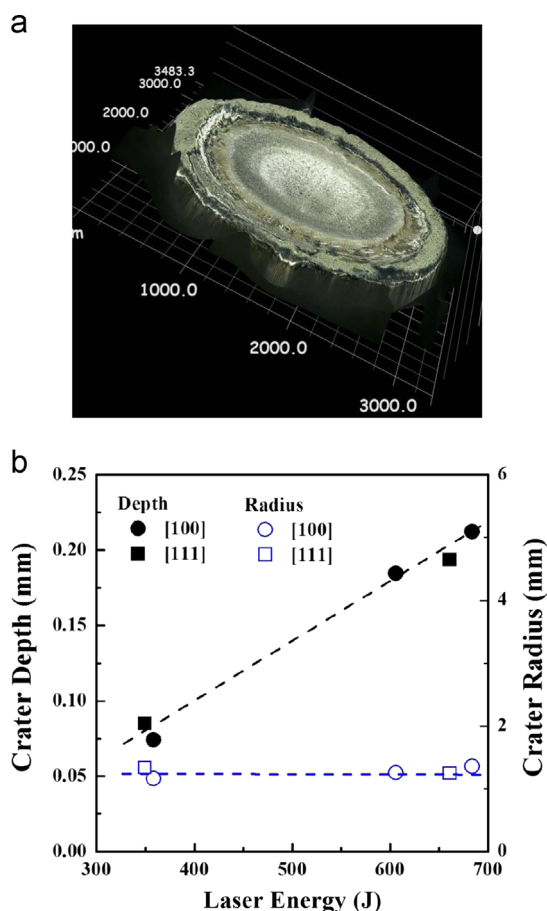
Fig. 5. (a) 3D crater view from digital microscope (Keyence VHX 1000); (b) Crater dimensions (depth and radius) as a function of laser energy.

two targets were used here, but three targets can potentially be fielded. The two targets were aligned along the H7–H14 and H3–H18 axis of the Omega target chamber and each driven by a cone of six symmetric beams fitted with SG8 phase plates (~900 μm spot diameter). The LiF witness target was along the H7–H14 axis in order to use the VISAR on TIM5 (Ten-inch-manipulator), H14 port and was driven by the H7 cone 1 beams (13, 66, 59, 67, 18, 24). The recovery target was mounted on a TIM (ten-inch manipulator) -based positioner (TIM3), aligned along H3–H18, and driven using the H3 cone 1 beams (56, 61, 55, 65, 58, 68). In a three-target geometry, another target can be positioned along the H3–H18 axis, opposite the recovery target. A model of the two-target geometry with propagating beams is shown in Fig. 3; both TIM5 and TIM3 directions are shown.

Previous attempts at measuring VISAR from a witness target while simultaneously driving a second sample target have resulted in loss of VISAR data due to a blanking effect in the LiF. The most likely causes of blanking are direct irradiation of the LiF by 1ω and 2ω laser light and x-ray irradiation of the LiF. To mitigate against both of these potential effects, the Al–LiF witness targets used in this study have a larger diameter Ta washer (10 mm OD, 2 mm ID compared to the 8 mm OD washer used on the recovery sample target) and a 3 mm long by 6 mm diameter Au cylinder surrounding the LiF.

3. Results and discussion

We briefly present the results of experiments conducted on the Omega Laser Facility on [100] crystal and nanocrystalline (g.s.~70 nm) Ta samples. Additionally, experiments were conducted with [110], [111], and [123] monocrystals and polycrystals at different laser energies. No momentum trap was used in the

[100] monocrystal experiments; however, both lateral and distal momentum traps were used (see Fig. 1(a)) for the nanocrystalline Ta. The detailed analysis and characterization are presented elsewhere [9,10].

3.1. Simulations

Experimental results from VISAR traces as well as simulations from two laser energy levels, 350 and 632 J, are shown in Fig. 4. Fig. 4(a) shows VISAR traces obtained at high (632 J) and low (350 J) drive energies on two separate shots. The dashed curves show the particle velocities of the Al–LiF interface derived from the VISAR data and the red solid curves are 1D simulations using LASNEX. Due to the nature of the 1D simulation, energy losses at the edges of the target are not taken into account. Thus, an arbitrary multiplier to the laser intensity was required in order to match the peak velocity. Each VISAR shot required a slightly different multiplier, ranging from 0.61 to 0.70. The data shown in Fig. 4(a) used multipliers of 0.70 and 0.63 for the 632 and 350 J shots, respectively. Since each shot, with the exception of one, had both a VISAR witness target and a recovery target, the multiplier derived from each of the VISAR traces were applied to the respective simultaneous Ta recovery targets when simulating the loading history of the recovered samples. The LASNEX calculations give a good match to the initial pressure rise, but diverge from the data after peak pressure. This has been shown to be due to poor release equation of state data for the CHBr (2%) reservoir material. However, we are mainly concerned with the peak pressures and the initial rate of pressure increase, both of which compare well with the data.

After obtaining a satisfactory match between simulations and the VISAR data, the Al–LiF was replaced by Ta in the simulation and the loading history of the recovered samples calculated. Fig. 4(b) shows the pressure vs. time calculated at a number of different depths from the front of the Ta sample recovered from the 632 J shot. The front of the Ta reached a peak pressure of ~110 GPa. The pressure profile stays quasi-isentropic until around 50 μm, at which distance the profile steepens into a shock. A more precise measure of the depth at which the profile steepens into a shock can be derived by looking at the ion temperature, T_{ion}, as a function of time at different depths from the front of the Ta, Fig. 4(c). A discontinuous jump in the ion temperature can be seen at and beyond 30 μm which is a clear indication of a shock. At distances less than 30 μm the increase is continuous.

3.2. Recovered Ta

We illustrate the effectiveness of this methodology through recovery experiments using tantalum monocrystals and nanocrystals. Tantalum is a model material for the BCC structure. The [100] orientation was chosen because it is the simplest to analyze. Each Ta specimen was mounted into the target assembly and subjected to laser compression with subsequent recovery. The monocrystals were subjected to 356, 606, and 684 J energy levels. These samples do not have accompanying VISAR traces, which were obtained in separate experiments at laser energy of 632 J and 350 J, Fig. 4(a). The pressure profiles for the recovery experiments can be calculated from these results by extrapolation. The pressure as a function of depth was simulated in 1D using a multiplier for the 632 J drive shot of 0.70 and is shown in Fig. 4(d). This multiplier was implemented by comparing VISAR traces with the computed predictions. These are upper-bounds on the peak pressures since energy losses at the edges of the target are not present in the 1D calculation.

Recovery Ta targets were characterized mainly by profilometry, scanning electron microscopy (SEM) and transmission electron microscopy (TEM). Fig. 5 shows a 3D image and the dimensions of

the crater. The crater depth increases monotonically with energy whereas the diameter of the crater is approximately constant. The same was observed for nanocrystalline tantalum, but the depth, at the same energy level, was lower. This is the result of the higher strength of the nanocrystalline material.

Fig. 6(a) shows SEM micrographs of the front of the Ta sample with the crater produced by the ICE drive. The crater profile can be seen more clearly from the cross-sectional view. The surface is covered with a mottled pattern that diverges from the center of energy deposition (shown in Fig. 6 by arrow pointing at erosion

lines). This is an erosional effect observed in all specimens. Superposed on this, many straight cracks are also observed on the crater surface (also marked by arrows in Fig. 6(a)) with a 90° pattern. The brittle nature of this fracture could be due to the rate at which it occurs, exceeding a ductile–brittle transition. Their orientation is consistent with intersection of {110} planes with the surface:{100}. Bubble structures are also observed after the crater surface was slightly electropolished. The schematic drawing is shown in the right side of Fig. 6(a). Similar damage was observed by Loomis et al. [11] on NiAl crystals subjected to laser shock.
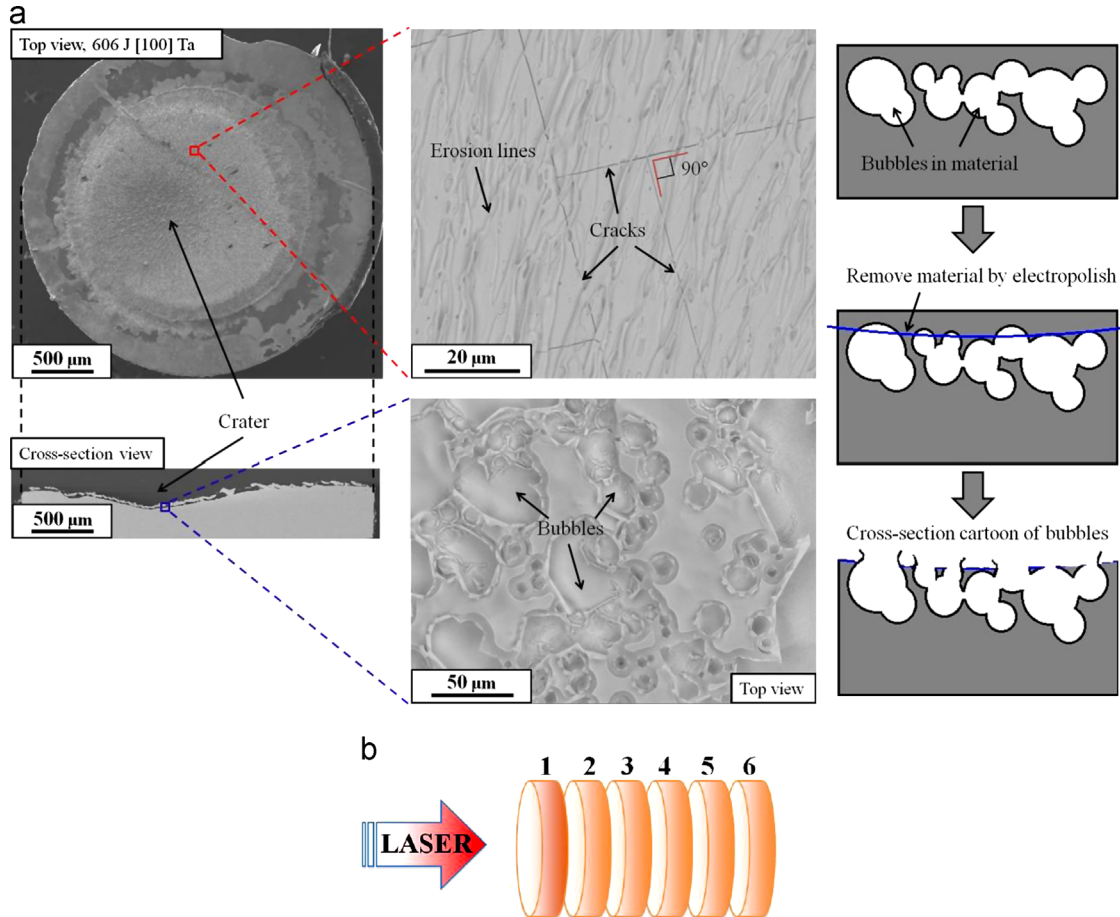

Fig. 6. (a) SEM micrographs of the drive crater of a recovered Ta [100] mono-crystal sample driven with 606 J to a peak pressure of ~100 GPa at the crater surface with top and cross-section view. Surface shows erosion marks and cracks (top) and bubbles (bottom). Sketches on right-hand side show bubble formation under the surface and their emergence as material is removed by electropolishing; (b) cartoon showing the post-shot sectioning of the Ta sample in relation to the laser drive direction. Each slice is ~250 μm thick.
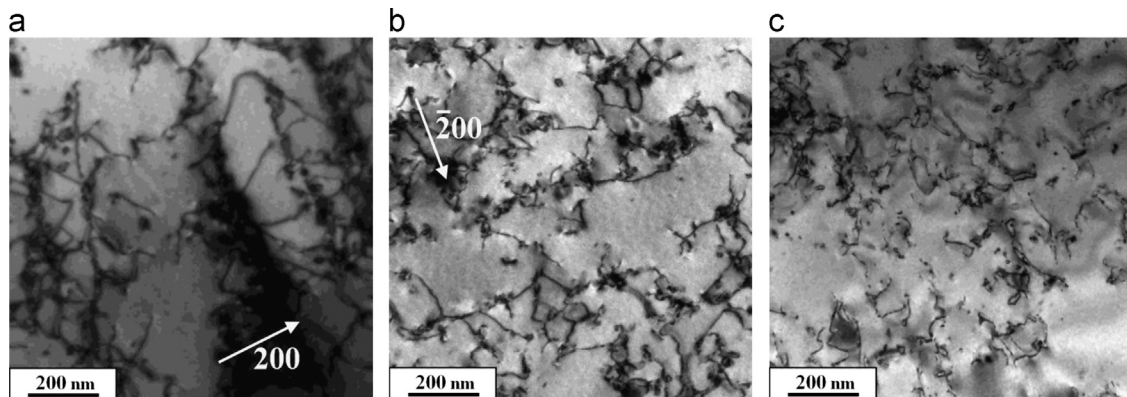

Fig. 7. TEM micrographs as a function of distance from the laser deposition surface for [100] Ta mono-crystal, driven with $E_{laser}=606$ J; (a) slice 3 (1.3 mm from laser impact surface; local pressure ~32 GPa); (b) slice 5 (2.2 mm from laser impact surface; local pressure ~21 GPa); (c) slice 6 (2.7 mm from laser impact surface; local pressure ~19 GPa).

However, the interpretation given by Loomis et al. [11], that they are due to reflected tensile pulses generated at the back surface, has to be discounted in our experiments. The thickness of the specimens (3 mm) was such that the wave has attenuated significantly once it reaches the back surface. Thus, the most probable cause for the cracks is tensile stresses due to contraction of the surface layers caused by cooling and/or melting.

The monocrystalline target was sectioned into 6 slices, ~250 μm thick, as shown in Fig. 6(b), for TEM analysis. Specimens were prepared by electropolishing. Depth-dependent deformation substructures were observed in slices 2, 3, 5, and 6 via TEM from $E_{Laser} = 606$ J [100] Ta target and are shown in Figs. 7 and 8. It should be emphasized that the pressure rise time decreases from the initial quasi-isentropic configuration in slice 1. Indeed, the LASNEX computations indicate that quasi-isentropic loading is restricted to a layer with ~30–40 μm thickness. From slices 3–6, all the TEM images show many dislocations; some of the dislocations organize themselves into deformation bands when their density reaches a critical level, as shown in Fig. 7(a). It is also observed that the dislocation
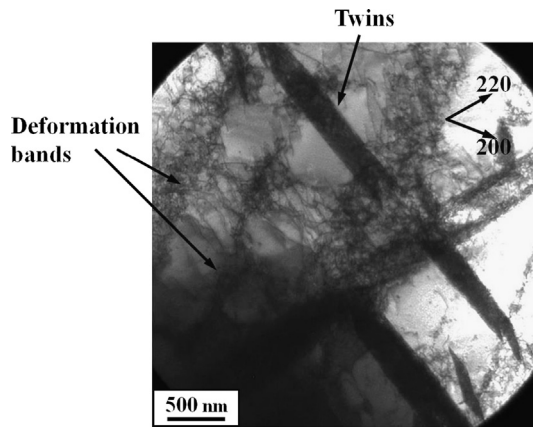

Fig. 8. TEM micrograph ([100] Ta single crystal, driven with $E_{laser} = 606$ J) at slice 2 (0.9 mm from laser impact surface; local pressure ~43 GPa).
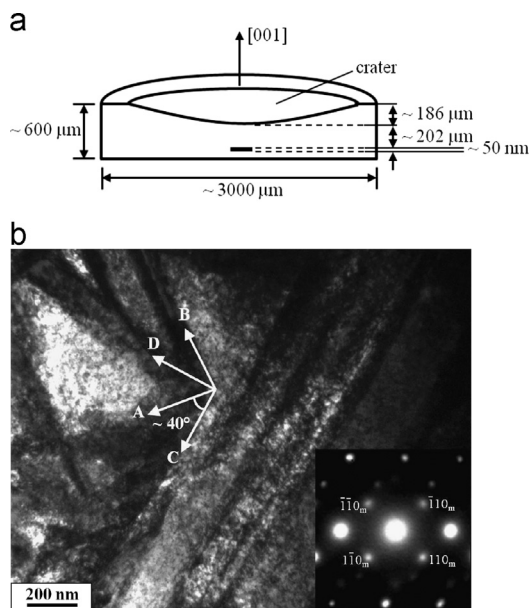

Fig. 9. (a) Schematic showing the location of focus ion beam (FIB) cutting in the slice 1 of [100] Ta mono-crystal, driven with $E_{Laser} = 606$ J. (b) TEM micrograph ([100] Ta single crystal, driven with $E_{laser} = 606$ J). FIB sample from slice 1 (0.4 mm from laser impact surface; local pressure ~68 GPa).

density decreases with distance from energy deposition surface. This is a direct result of the pressure decay, predicted in Fig. 4(d).

The deformation structure viewed in slice 2 shows twins, in conjunction with deformation bands (Fig. 8). A slip-twinning transition occurs when the pressure exceeds a threshold value. This behavior has been seen earlier for copper [25] and flyer-plate shocked tantalum [26]. The experimental results show that the slip-twinning transition threshold [9,25,26,30] is confined between slice 2 and 3, which corresponds to a pressure range 32–43 GPa. The Focused Ion Beam (FIB) technique was also used for thinning slice 1 and the result is shown in Fig. 9. Comparing Fig. 8 and Fig. 9(b), a higher twin density was obtained with higher pressure. Based on the similar Schmid factor for {112} and {123} planes for energy deposition direction [001], and the angle between two perpendicular set of twin structures in Fig. 9(b), the twin structures were generated not only on {112} planes, but also {123} planes. In addition, a pressure-induced BCC-HCP transition was observed above ~70 GPa, corroborating results by Hsiung [27–29].

The region undergoing quasi-isentropic loading required a different specimen preparation and analyzing method. The back-scattered SEM (BSE) of the crater bottom is shown in Fig. 10(a); no clear substructures were observed. This can be a thermal effect, since the temperature reaches high levels and the deformation structure is annealed away. By successive electropolishing steps, profilometry measurement, and BSE characterization, the deformation structure as a function of depth could be established. The first deformation substructure was observed as shown in Fig. 10(b) and the structures in the enlarge figure is similar to Fig. 9(b) with featured by two sets of perpendicular structures with angle between them about 40°. From profilometry measurement, the structures shown in Fig. 10 (b) are at ~42 μm beneath the crater depth. The isentropic loading penetrates only ~42 μm into the samples because the steepening of the pulse builds a shock wave. This is consistent of the simulation results previous discussed and shown in Fig. 4. We observed clear differences in the microstructure between the isentropic and the shock-compressed region. An in-depth analysis of samples will be published elsewhere [10].

The deformation structure of the nanocrystalline tantalum was quite different from the monocrystals [10]. No twins were observed, even at the highest pressures, showing that the slip-twinning transition stress is dependent on grain size. The dislocation density observed in the grains is also lower than the one observed in the monocrystals. Fig. 11 shows grain boundaries and dislocations in the nanocrystalline sample imaged in both bright (left) and dark field (right). The difference with the monocrystalline sample (e.g., Fig. 8) is evident.

4. Conclusions

A soft-recovery setup for quasi-isentropically compressed samples was designed and successfully fielded on the Omega laser. It was used in a number of Ta monocrystalline and nanocrystalline samples. Simultaneous VISAR was obtained from Al–LiF witness targets with no sign of blanking and the Al particle velocity simulated in one dimension using LASNEX. Pressure profiles as a function of time and depth into in the Ta samples were also calculated using the laser intensity scaling factors derived from the VISAR data.

We observed that the high pressure (~100 GPa) Ta samples penetrated into the Aerogel while low-pressure samples (~30 GPa) did not, i.e. the pressure applied by the incoming Ta target was not great enough to overcome the compressive strength of the aero gel. The "snowplow" calculations for aero gel penetration are very sensitive to the compressive strength of aero gel, for which there is little data. Nevertheless, the low pressure targets were still recovered due to being trapped between the top of the aero gel and the Ta
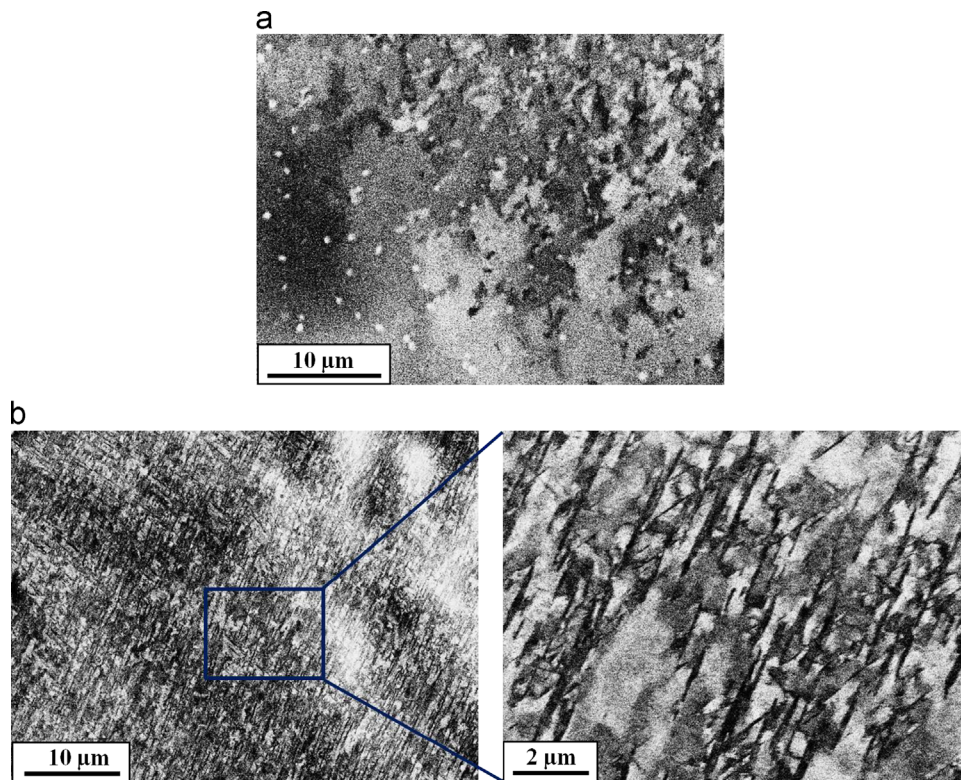
Fig. 10. Macrographs by SEM-BSE (20 kV) in [100] Ta at $E_{Laser}=606$ J; (a) surface of the crater bottom; (b) surface after removing ~42 μm by electropolishing showing twins and deformation microstructure first observed.
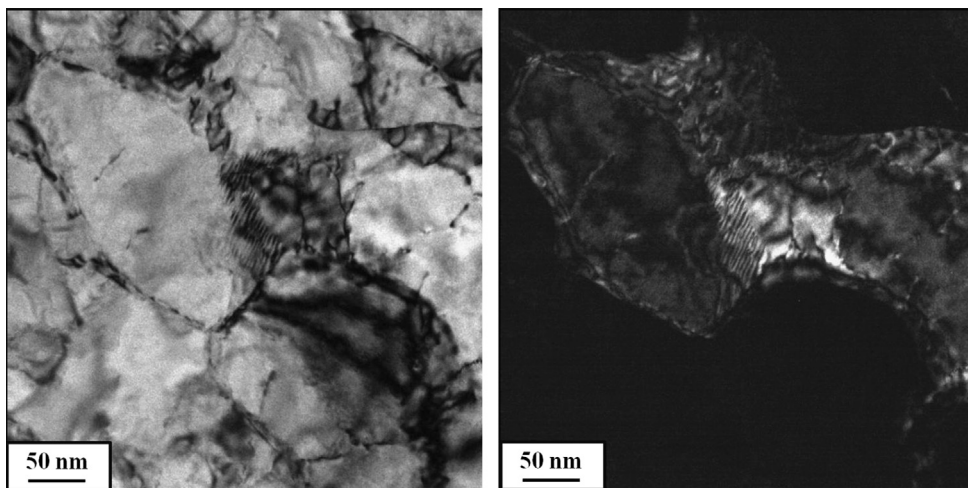

Fig. 11. Dislocations generated in nanocrystalline tantalum at laser energy of 662 J and 1.6 mm from surface imaged in both bright and dark field.

washer. Future experiments will utilize a lower density aero gel to ensure proper soft recovery of low pressure targets and will be used to calibrate the penetration models at low aero gel density.

The experimental procedure described here can be applied to any material-metal, ceramic, or polymer- to establish the governing plasticity and damage mechanism s under these extreme conditions of pressure (up to and even above 100 GPa) and strain rate (up to 10^9 s^{-1}).

References

[1] J.M. McNaney, M.J. Edwards, R. Becker, K.T. Lorenz, B.A. Remington, Metall. Mater. Trans. A 35A (2004) 2625.
[2] M.S. Schneider, B. Kad, D.H. Kalantar, B.A. Remington, E. Kenik, H. Jarmakani, M.A. Meyers, Int. J. Impact Eng. 32 (2005) 473.
[3] B.A. Remington, P. Allen, E.M. Bringa, J. Hawreliak, D. Ho, K.T. Lorenz, H. Lorenzana, J.M. McNaney, M.A. Meyers, S.W. Pollaine, K. Rosolankova, B. Sadik, M.S. Schneider, D. Swift, J. Wark, B. Yaakobi, Mater. Sci. Technol. 22 (2006) 474.
[4] D.H. Kalantar, J. Belak, E. Bringa, K. Budil, M. Caturla, H. Colvin, M. Kumar, K.T. Lorenz, R.E. Rudd, J. Stolken, A.M. Allen, K. Rosolankova, J.S. Wark, M.A. Meyers, M.S. Schneider, Phys. Plasma 10 (2003) 1569.
[5] Y.M. Wang, E.M. Bringa, J.M. McNaney, M. Victoria, A. Caro, A.M. Hodge, R. Smith, B. Torralva, B.A. Remington, C.A. Schuh, H. Jarmakani, M.A. Meyers, Appl. Phys. Lett. 88 (2006) 061917.
[6] M.A. Meyers, F. Gregori, B.K. Kad, M.S. Schneider, D.H. Kalantar, B.A. Remington, G. Ravichandran, T. Boehly, J.S. Wark, Acta Mater. 51 (2003) 1211.

[7] M.A. Meyers, M.S. Schneider, H. Jarmakani, B. Kad, B.A. Remington, D. H. Kalantar, J. McNaney, B. Cao, J. Wark., Metall. Mater. Trans. A 39A (2008) 304–324.

[8] H.N. Jarmakani, E.M. Bringa, P. Erhart, B.A. Remington, Y.M. Wang, N.Q. Vo, M.A. Meyers, Acta Mater. 56 (2008) 5584.

[9] C.-H. Lu, B.A. Remington, B.R. Maddox, B. Kad, H.S. Park, S.T. Prisbrey, M.A. Meyers, Acta Mater. 60 (2012) 6601.

[10] C.-H. Lu, B.A. Maddox B.R. Maddox, B. Kad, H.S. Park, T.G. Langdon, M. Kawasaki, M.A. Meyers, Unpublished results (2013).

[11] E. Loomis, D. Swift, P. Peralta, K. McClellan, Mater. Sci. Eng. A 404 (2005) 291–300.

[12] J. Edwards, K.T. Lorenz, B.A. Remington, S. Pollaine, J. Colvin, D. Braun, B.F. Lasinski, D. Reisman, J.M. McNaney, J.A. Greenough, R. Wallace, H. Louis, D. Kalantar, Phys. Rev. Lett. 92 (2004) 075002.

[13] K.T. Lorenz, M.J. Edwards, A.F. Jankowski, S.M. Pollaine, R.F. Smith, B.A. Remington, High Energy Density Phys. 2 (2006) 113.

[14] T.R. Boehly, R.S. Craxton, T.H. Hinterman, J.H. Kelly, T.J. Kessler, S.A. Kumpan, S.A. Letzring, R.L. McCrory, S.F.B. Morse, W. Seka, S. Skupsky, J.M. Soures, C.P. Verdon, RScI 66 (1995) 508.

[15] L.M. Barker, R.E. Hollenbach, JAP 43 (1972) 4669.

[16] G. Zimmerman, D. Kershaw, D. Bailey, J. Harte, J. Opt. Soc. Am. 68 (1978) 549.

[17] P.S. DeCarli, M.A. meyers, Design of Uniaxial Strain Shock Recovery Experiments, in Shock waves and High-Strain-Rate Phenomen in metals, Plenum, NY, 1981pp. 341–374, (Chapter 22).

[18] G.T. Gray III, Influence of shock-wave deformation on the structure/property behavior of materials, in: J.R. Asay, M. Shahinpoor (Eds.), High-Pressure Shock Compression of Solids, Springer, New York, 1993, pp. 187–216.

[19] G.T. Gray III, P.S. Follansbee, C.E. Frantz, Mater. Sci. Eng. A 111 (1989) 9–16.

[20] G.T. Gray III, Shock wave testing of ductile materialsin: H. Kuhn, D. Medlin (Eds.), ASM Handbook: Mechanical Testing and Evaluation, vol. 8, ASM International, Materials Park, OH, 2000pp. 530–538.

[21] N.K. Bourne, G.T. Gray III, Proc. Roy. Soc. Math. Phys. Eng. Sci. 461 (2005) 3297–3312.

[22] R.E. Tokheim, D.C. Erlich, D.R. Curran, M. Tobin, D. Eder, Proceedings of AIP Conference, (2004).

[23] D. Eder (private communication), 2008.

[24] ⟨http:/www.lle.rochester.edu/omega_facility/omega/⟩.

[25] M.S. Schneider, F. Gregori, B.K. Kad, D.H. Kalantar, B.A. Remington, M.A. Meyers, Proceedings of AIP Conference Proceedings, (2004).

[26] L.E. Murr, M.A. Meyers, C.S. Niou, Y.J. Chen, S. Pappu, C. Kennedy, Acta Mater. 45 (1997) 157.

[27] L.M. Hsiung, D.H. Lassila, Scr. Mater. 38 (1998) 1371.

[28] L.M. Hsiung, D.H. Lassila, Acta Mater. 48 (2000) 4851.

[29] L.M. Hsiung, J. Phys.Condens. Matter 22 (2010) 385702.

[30] G.T. Gray, K.S. Vecchio, Metall. Mat, Trans. A 26 (1995) 2555.